PHYSICAL REVIEW MATERIALS **5**, 053602 (2021)

Probing the small-scale plasticity and phase stability of an icosahedral quasicrystal i-Al-Pd-Mn at elevated temperatures

Changjun Cheng,[1] Yuan Xiao,[2] Michel J. R. Haché,[1] Zhiying Liu,[1] Jeffrey M. Wheeler,[2] and Yu Zou[1,*]

[1]*Department of Materials Science and Engineering, University of Toronto, 184 College Street, Toronto, Ontario, Canada M5S 3E4*

[2]*Laboratory for Nanometallurgy, ETH Zurich, HCI F 538, Vladimir-Prelog-Weg 5, CH-8093 Zurich, Switzerland*

(Received 26 December 2020; accepted 20 April 2021; published 6 May 2021)

Quasicrystalline materials possess a unique structure that is ordered yet not periodic. Despite their special configuration and many useful properties, they are typically very brittle at temperatures below ∼75% of their melting points, rendering them difficult to process and often unsuitable for practical implementations. Microcompression offers an opportunity to unveil the fundamental mechanisms of quasicrystal plasticity. Here, we study the mechanical behavior of a typical icosahedral quasicrystal (i-Al-Pd-Mn) using microthermomechanical techniques over a temperature in the range 25–500 °C. We observe a few interesting phenomena, including micropillar shrinkage, phase transformations, grain refinement, and thermally induced transitions in deformation behavior (from brittle fracture at room temperature to serrated plastic flows and then to homogeneous flows at elevated temperatures). Furthermore, we discuss the multiple underlying mechanisms on the mechanical behavior of the quasicrystal in this temperature regime, exploring surface evaporation/diffusion, diffusion-enhanced plasticity, dislocation activities, and grain boundary rotation/sliding. Our study bridges the gap between room-temperature and high-temperature plasticity in quasicrystals, demonstrating an opportunity to study complex intermetallic phases in broad size and temperature regimes.

DOI: 10.1103/PhysRevMaterials.5.053602

I. INTRODUCTION

Quasicrystals (QCs), or quasiperiodic crystals, are a class of materials that exhibit long-range order in their atomic arrangement but lack translational symmetry (periodicity) in at least one dimension [1,2]. QCs can possess fivefold, tenfold, and twelvefold symmetries that are forbidden according to the classical theorems of crystallography [3–5]. Conventionally, a crystal is defined as a regular array of atoms, repeating periodically in the space [6], i.e., an infinite 3D periodic arrangement of identical structure motifs [7]. In reciprocal space, only the point symmetry between structure factors is maintained, leading to a crystal definition $n > 3$ dimensions [7]; quasicrystals can be described as an n-dimensional periodic structure with a lattice of higher symmetry in superspace, therefore they can still be classified as a unique type of crystal, albeit aperiodic crystals [2]. For example, decagonal QCs show periodically stacked two-dimensional quasiperiodic layers along tenfold symmetry [8], while icosahedral QCs contain fivefold symmetry axes and show quasiperiodicity in three dimensions [9]. Since the discovery of QCs in the 1980s [1], many QCs were discovered in laboratories [10–15] through a methodical study of phase diagrams and guiding principles such as e/a ratio based on Hume-Rothery laws and atomic size ratios [16]. Some QCs are also found in nature [17,18]. Owing to their unique quasiperiodic structure, QCs exhibit many interesting and unusual properties, including high hardness [19,20], low friction coefficients [21,22], strong light absorption [23], high hydrogen storage [24], low thermal conductivities [15], and many special magnetic and electronic properties [25–28]. Despite these useful properties, the practical use of QCs remains very limited. The main drawback that prevents their broad application is their brittleness at room temperature (RT) and elevated temperatures (approximately 25–600 °C) [19,29,30]. Conventionally, steady plasticity in QCs can only be achieved at high temperatures (above approximately 600 °C, or above ∼75% of their melting temperatures [31,32]) or under confining hydrostatic pressures [33,34]. To date, the mechanical behavior of QCs in the elevated temperature regime is still poorly understood—much in contrast to crystalline and amorphous solids.

In addition to phonon components in regular crystal dislocations, dislocations in QCs also contain phason components [35,36], which are supplementary long wavelength excitations related to the perpendicular subspace of six-dimensional hyperspace [37–39], leading to structural and chemical disorder in physical space [40]. The phason strain is the perpendicular component of the six-dimensional displacement that causes matching-rule violations in the corresponding quasilattice, in which certain atoms disappear and emerge in unexpected places [39]. Therefore, the discontinuity from phason defects results in a shift of weaker diffraction peaks away from the ideal position. The propagation of dislocations in QCs is significantly hindered by phason strains, resulting in poor ductility at RT, and even elevated temperatures [37]. At high temperatures, phason faults become unstable and tend to vanish rapidly by diffusion [41,42], and the dislocations are able to overcome the phason drag through thermally activated processes such as dislocation climb [43–45]. Previous studies of QC plasticity have concentrated on i(cosahedral)-Al-Pd-Mn [40,46], i-Al-Cu-Fe [47], and d(ecagonal)-Al-Ni-Co [31].

---

[*] Corresponding author: mse.zou@utoronto.ca

©2021 American Physical Society

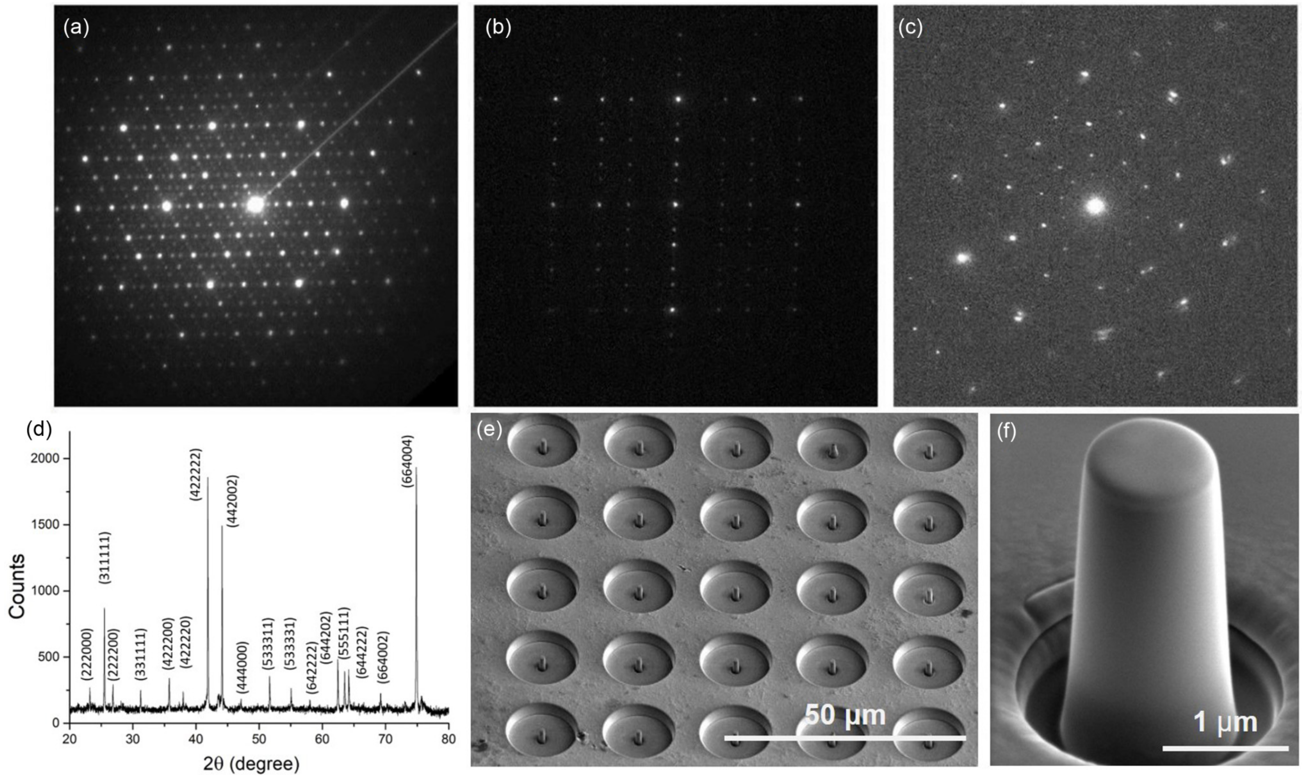

FIG. 1. TEM electron diffraction patterns for the i-Al-Pd-Mn crystal along (a),(b) twofold and (c) fivefold symmetry axes [48]; (d) powder diffraction (Cu, $K\alpha 1$) pattern for the as-cast i-Al-Pd-Mn ingot. SEM images of (e) the array matrix of FIB-milled pillars produced in one large grain; and (f) a micropillar before compression (approximately 1 μm in diameter).

Recently, Zou and his co-workers showed that i-Al-Pd-Mn [48] and d-Al-Ni-Co [49] QCs could exhibit good plasticity, even at room temperature, when their dimensions are reduced to the submicrometer scale ($<\sim$500 nm) using the microcompression and microbending methods. This small-scale mechanical testing technique enables the investigation of plastic behavior of typically brittle QCs by suppressing fracture before plastic yielding occurs. Very recently, Zou *et al.* [50] also reported on the mechanical properties of a d-Al-Ni-Co quasicrystal at temperatures up to 600 °C, using an elevated temperature micromechanical testing system. The d-Al-Ni-Co quasicrystal showed a clear brittle-to-ductile transition upon loading within 25–600 °C region and maintained a stable d-QC structure [50]. However, the mechanical investigation of i-Al-Pd-Mn from 25 to ~500 °C is more challenging than that of d-Al-Ni-Co. First, to our best knowledge, there is little knowledge of the phase diagram of the Al-Pd-Mn system below 650 °C in the literature [51,52]. Second, the mobility of the constituent atoms, Al, Pd, and Mn, is considerably increased at the elevated temperatures, especially above ~300 °C, resulting in more complex deformation phenomena. Third, a stable phase can be observed after the deformation at room temperature to 300 °C [53–55], while the existence of polycrystalline structure at 480 °C implies the occurrence of phase transformation [56,57]. Thus, a fundamental question arises: What are the mechanical behavior, phase stability, and corresponding underlying mechanisms of the i-Al-Pd-Mn deformed at the temperature range from 25 to 500 °C? In this study, through the microthermomechanical testing of i-Al-Pd-Mn, we seek to unveil its deformation mechanisms in the temperature in the range 25–500 °C, providing an improved fundamental understanding of the plastic deformation of quasicrystals.

II. MATERIALS AND METHODS

A. Sample preparation and characterization

An $Al_{70}Pd_{21.5}Mn_{8.5}$ sample was produced from pure metals (99.9999% Al, 99.9% Pd, and 99.95% Mn) by arc melting and was subsequently heat treated in a quartz capsule under a protective Ar atmosphere. The heat treatment procedure was conducted as follows: (1) heating to 1050 °C (above the melting temperature of $Al_{70}Pd_{21.5}Mn_{8.5}$); (2) slow cooling to 810 °C at a rate of 30 °C per hour; (3) annealing at 810 °C for 150 h; and (4) quenching in water. The QC structure of the as-prepared i-Al-Pd-Mn ingot was determined by powder x-ray diffraction (XRD, Panalytical X´Pert PRO) and then verified by selected area electron diffraction (SAED) in a transmission electron microscope (TEM, Thermofisher Scientific, Talos F200X), indicating that the ingot consisted of a few single quasicrystals having an icosahedral structure [Figs. 1(a)–1(d)], which has been confirmed in our previous study [48]. Energy dispersive x-ray spectroscopy (EDS) was performed in a scanning transmission electron microscopy (STEM, gun lens 6, spot size 4, camera length 0.098 m) mode of the TEM instrument, which revealed a homogeneous composition throughout the sample volume.

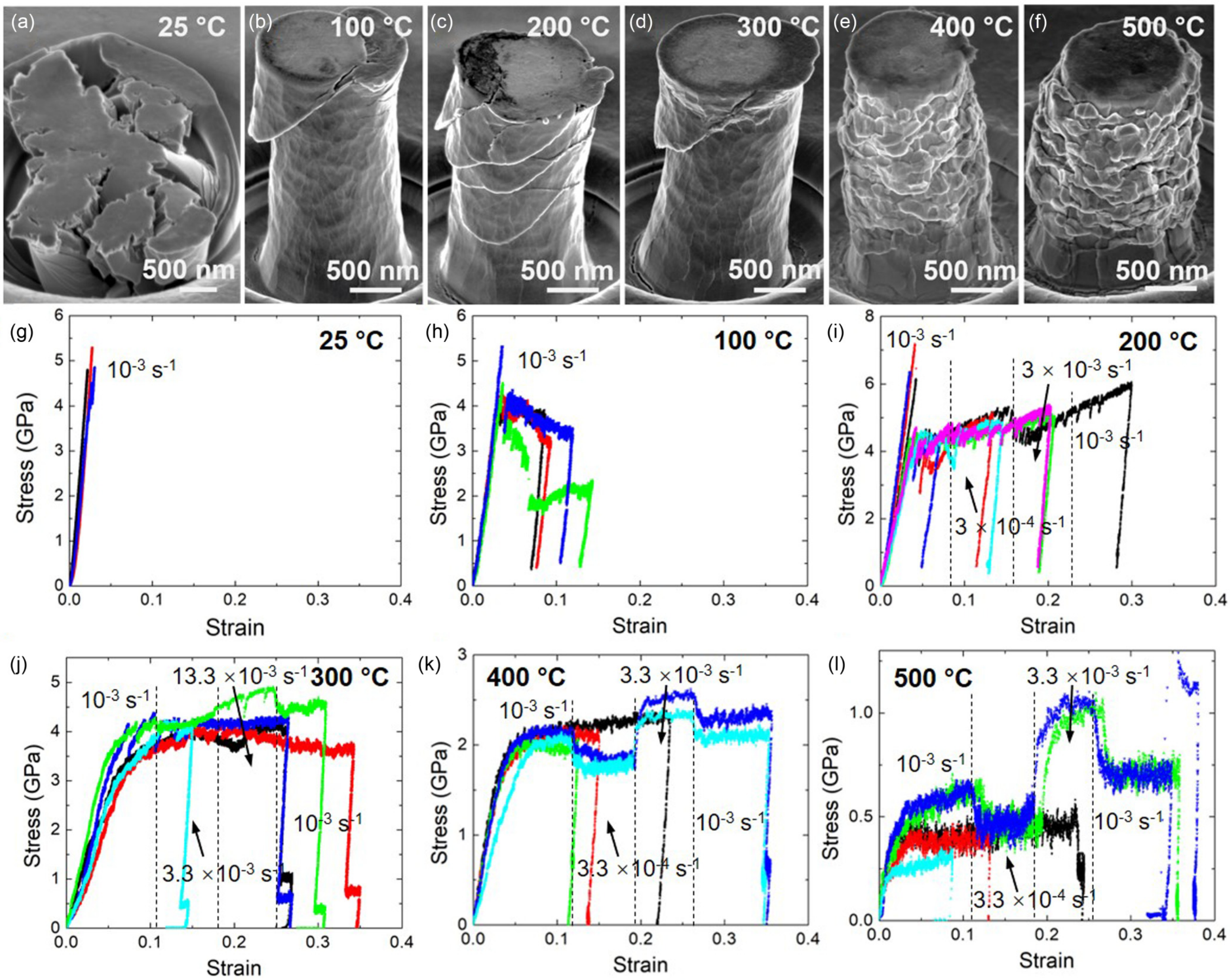

FIG. 2. Representative SEM (SE: secondary electron) micrographs of i-Al-Pd-Mn micropillars after compression experiments at (a) 25, (b) 100, (c) 200, (d) 300, (e) 400, and (f) 500 °C. Panels (g)–(l) show the corresponding stress-strain curves for the pillars deformed in this temperature range. An initial constant strain rate of $10^{-3}\,\mathrm{s}^{-1}$ was used, and compression was carried out at 200–500 °C at strain rate jumps of $3.3 \times 10^{-4}\,\mathrm{s}^{-1}$ and $3.3 \times 10^{-3}\,\mathrm{s}^{-1}$.

The ingot was polished consecutively using a 3-μm diamond paste and a 60-nm colloidal silica suspension, after which 25 single-quasicrystalline cylindrical pillars of uniform size were fabricated in single grain using a focused ion beam (FIB) system (Helios Nanolab 600i, Thermo Fisher Scientific). Coarse milling was first performed using steadily decreasing ion currents down to 80 pA (Ga+ at 30 kV), followed by final polishing using 7 pA (Ga+ at 30 kV). Both the undeformed and deformed pillars were imaged using a high-resolution (HR) scanning electron microscope (SEM) (Magellan 400, Thermofisher Scientific). Before deformation, the top diameters of the FIB-milled pillars were approximately 1 μm with a taper of about 3 ° and an aspect ratio of about 3–4.5, as shown in Figs. 1(e) and 1(f). TEM specimens were prepared as TEM lamellae using FIB milling. Prior to lamellae milling, the pillar surfaces were protected by FIB-assisted deposition of an amorphous carbon layer. Thinning down to electron transparency of the lamellae was performed at 5 kV of Ga+ and 3 kV of the electron source potentials.

B. Micromechanical testing at room and elevated temperatures (25–500 °C)

An *in situ* nanoindenter (Alemnis, Switzerland) with a 5-μm-diameter diamond flat punch tip (Synton-MDP, Switzerland) was used in an SEM (Vega 3, Tescan) to compress the micropillars using displacement control in the temperature in the range 25–500 °C under an SEM vacuum condition ($\sim 10^{-6}$ Pa). The indenter was modified by incorporating independent tip and sample heating with a water-cooled frame. Due to the thermally stable system frame and the precise matching of the sample and indenter temperatures, the typical thermal drift values were less than $0.02\,\mathrm{nm\,s^{-1}}$. Engineering stresses were calculated based on the top diameters of each pillar. Three to four pillars were tested at

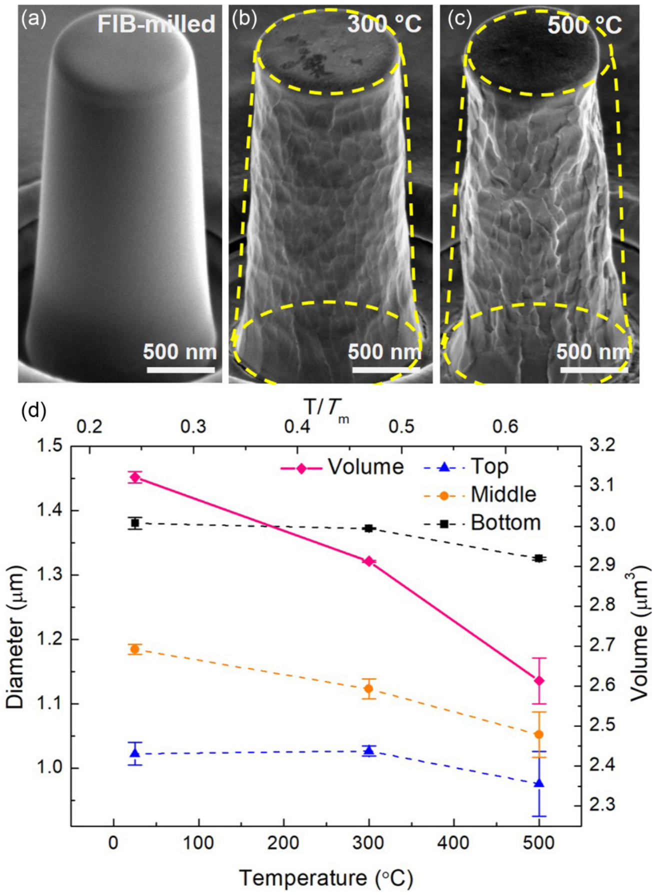

FIG. 3. SEM micrographs showing the morphologies of undeformed pillars after different testing stages: (a) as-milled, (b) annealed at 300 °C, and (c) annealed at 500 °C. (d) Corresponding diameters and volumes of the undeformed pillars after annealing. The average decrease of the pillar volume is 0.14 μm^3 (4.5%) and 0.42 μm^3 (13.8%) for 300 and 500 °C, respectively. The melting point (T_m) of the i-Al-Pd-Mn is about 950 °C (1223 K).

each temperature (25, 100, 200, 300, 400, and 500 °C), while five pillars were heated and left undeformed to serve as comparisons.

Testing was arranged in three stages. The first set of tests was performed at 25 °C. The second set of tests was performed at 100, 200, and 300 °C; at each new temperature, the sample was held for about one hour to ensure the thermal stability (no thermal drift) before testing. The sample was then removed from the SEM chamber (Vega 3) after testing at 300 °C and imaged using an HR SEM (Magellan 400). The third set of tests was performed at 400 and 500 °C. The holding time for these tests was extended to 1.5–2 h, and the deformed samples were again transferred from nanoindenter setup to the SEM for imaging. The average time for each set of tests at a single temperature increment (including heating, thermal stabilization, and deformation) was about 2.5 h. The initial strain rate was $10^{-3}\ \text{s}^{-1}$ for all micropillars. To analyze the strain rate sensitivity (SRS), strain rate jump patterns were adjusted during testing at each temperature to accommodate the changes of flow characteristics: (i) 200 °C: $(1, 0.3, 3) \times 10^{-3}\ \text{s}^{-1}$; (ii) 300 °C: $(1, 3.3, 13.3) \times 10^{-3}\ \text{s}^{-1}$; and (iii) 400 and 500 °C: $(1, 0.33, 3.3) \times 10^{-3}\ \text{s}^{-1}$. Since all the pillars were prepared from the same bulk QC ingot (within the same large QC grain) and setting up the elevated temperature microcompression testing is very time consuming, only the samples tested at room temperature and 500 °C were characterized in TEM.

III. RESULTS

A. Micropillar compression in the temperature in the range 25–500 °C

Figure 2 shows the representative SEM micrographs and corresponding engineering stress-strain curves of the compressed micropillars. At 25 °C, the micropillars underwent catastrophic failure at about 3% strain without detectable plasticity [Figs. 2(a) and 2(g)], as the pillars fractured into several pieces. Rising deformation temperature resulted in an increase in plasticity. Two types of the deformed pillar surface morphologies were observed at the test: wrinkles below and at 300 °C, and protrusions at compressions above 300 °C. It is noted, however, that the whole set of samples for temperature-dependent compressions within the 25–300 °C range was staying in the SEM chamber on the stage during all the tests. This could indicate that all wrinkled features in specimens deformed at $T < 300$ °C might be the consequence of heating to and holding at 300 °C during the compression tests. Deformation bands declined at ∼45 ° relative to the loading axis are observed in the pillars tested between 100 and 300 °C [Figs. 2(b)–2(d)], while at 400–500 °C the pillars exhibit no traces of deformation bands but distinctly rough surface morphology with protruding features about 150 nm in size [Figs. 2(e) and 2(f)]. This morphology transition between 300 and 400 °C could be correlated to the phase transformation, indicating a decomposition of the single QC structure, which is discussed further in Sec. III C 3. The engineering stress-strain curves exhibit serrated plastic flow behavior at 100, 200, and 300 °C [Figs. 2(g)–2(i)], in which obvious displacement burst, a common phenomenon observed in microcompression of metal [58,59], is also observed in the stress-strain curves of the pillars deformed at 100 and 200 °C. The pillars deformed at 400 and 500 °C exhibited relatively more homogeneous plastic flow and showed the increased and positive SRS [Figs. 2(k) and 2(l)]. The flow stresses of the pillars significantly decreased when tested above 300 °C, implying a transition of deformation mechanism.

B. Annealed (undeformed) micropillars after 300 and 500 °C

To compare thermally and thermomechanically induced effects, the undeformed pillars were annealed and analyzed in SEM. Figures 3(a)–3(c) show a substantial decrease in the pillar volume (shrinkage) with increasing temperature, a phenomenon that was not reported in the elevated temperature microcompression of d-Al-Ni-Co [50]. Figure 3(d) shows the corresponding changes in diameters and volumes of pillars thermally treated at different temperatures. The approximate volume loss for pillars annealed at 300 and 500 °C are 0.14 μm^3 (4.5%) and 0.42 μm^3 (13.8%), respectively. Both the annealed pillars showed a wrinkled surface morphology, which is more prominent in the 500 °C annealed pillar. The micrographs show that the wrinkle pattern is uniformly

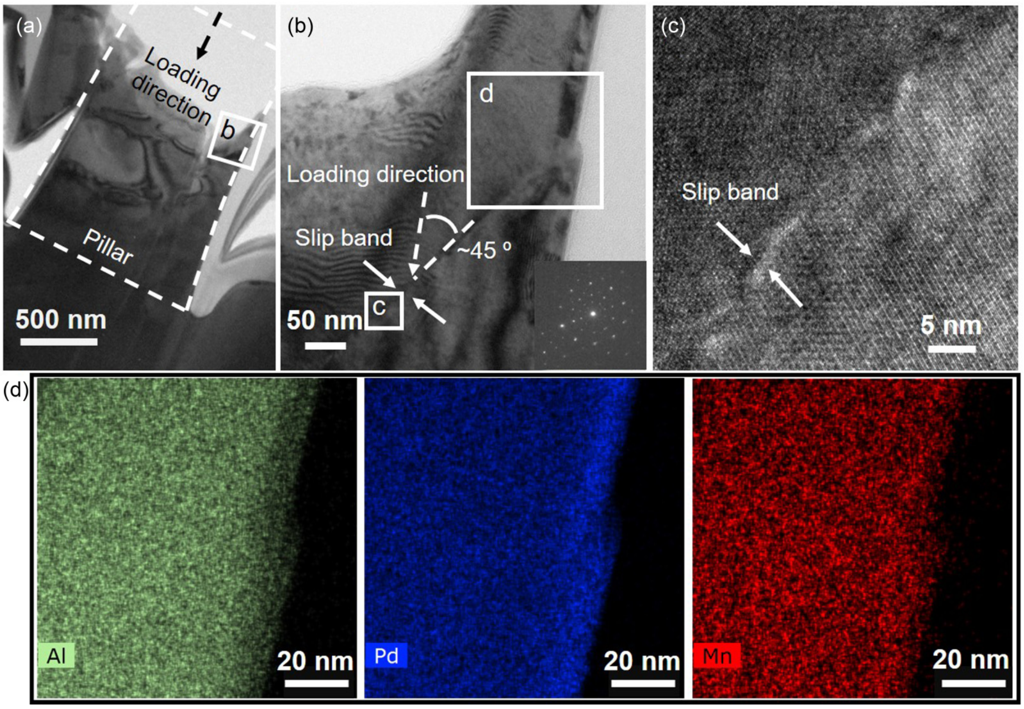

FIG. 4. (a),(b) Representative TEM and (c) HR TEM micrographs, and (d) corresponding elemental maps acquired from compressed pillar loaded just up to the point of fracture at room temperature. The highly localized slip band in (b) and (c) is at about 45 ° from the loading axis. The uniformly elemental distribution indicates no phase separation in the specimen.

distributed on the pillar surfaces, suggesting the decomposition of quasicrystalline structure to polycrystalline form upon annealing without any mechanical loading.

C. TEM microstructural analysis

1. Micropillars deformed at room temperature

Figures 4(a) and 4(b) show the bright field TEM (BF TEM) micrographs of a QC pillar compressed at 25 °C. The dashed line in Fig. 4(a) presents the original shape of the as-milled pillar before compression. The contrast modulations in the pillar body are induced by compression rearrangement of lattice defects that resulted in the formation of the pillar regions differently oriented towards the electron beam. The dark area at the bottom of the pillar is too thick to resolve any microstructure features. The diffraction contrast in Fig. 4(b) shows a region at the top of the pillar and reveals a slip band terminating at the surface. The high-resolution TEM (HR TEM) image in Fig. 4(c) shows that the slip band is very sharp (about 2–3 nm in thickness) and is oriented at about 45 ° to the loading direction. This localized plasticity matches well with the results of bulk i-Al-Pd-Mn specimens deformed at low temperatures [53–55]. The diffraction pattern in the inset of Fig. 4(b) confirms that the QC structure of the pillar remained unchanged upon deformation. Moreover, the element distribution maps by EDS [Fig. 4(d)] also show a uniform distribution of Al, Pd, and Mn in the pillar body with only a minor chemical content modulation at the pillar surface (higher Pd and weaker Al signals) at the pillar surface. Therefore, no phase transformation occurred during room-temperature compression of the i-Al-Pd-Mn.

2. Micropillars annealed at 500 °C (undeformed)

Figure 5 presents TEM micrographs of undeformed pillars heat-treated at 500 °C for about 3 h. The high-angle annular dark-field (HAADF) STEM mode [Figs. 5(a) and 5(c)] demonstrates the elemental content modulations in the annealed sample: the brighter areas in the HAADF image show the regions with a heavier element, Pd, whereas the darker areas correspond to Pd-depleted regions. The EDS elemental content distribution maps from the same pillar (Fig. 6) confirm the multiphase state of the annealed pillar. Furthermore, the contrast modulations (darker and brighter gray regions) in the BF TEM images [Figs. 5(b), 5(d), and 5(e)] also confirm that the microstructural evolution can be caused by the heat treatment. These images clearly reveal the polycrystalline characteristics with average grain size (d_{Avg}) of about 240 nm. The diffraction analyses of the pillar, shown in the insets of Figs. 5(b) and 5(e), confirm the presence of non-QC structures. The existence of the Al_3Pd_2 phase (hP5, SG P-3m1) is verified by the SAED analyses (Supplemental Material Fig. S1 [60]) and is confirmed by the composition EDS STEM analyses of the same regions. The analyses of the fast Fourier transform (FFT) patterns acquired from the regions in the HR TEM images, for example, Figs. 5(f) and 5(g), also indicate the presence of Al_3Pd_2 (hP5, SG P-3m1) and AlPd (hR26, SG R-3) phases (Supplemental Material Fig. S2). The FFT patterns from other regions (Supplemental Material Figs. S3 and S4) confirm the presence of Al_8Mn_5 (hR52, SG R3m) and remaining icosahedral $Al_{68.5}Pd_{22.1}Mn_{9.4}$ phases [61,62]. We conclude that 500 °C annealing of the icosahedral $Al_{70}Pd_{21.5}Mn_{8.5}$ alloy results in phase decomposition and the transformation into a multiphase state.

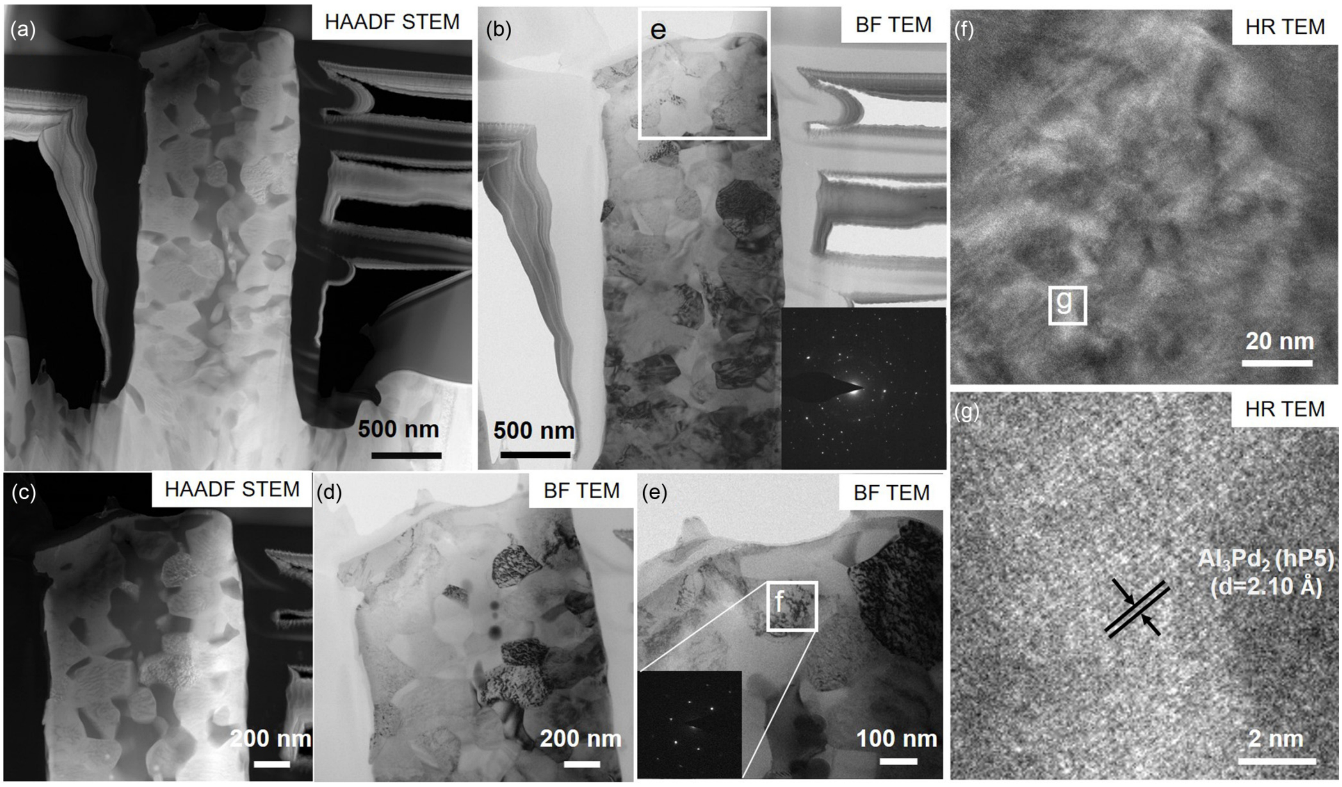

FIG. 5. (a),(c) HAADF STEM, (b),(d),(e) BF TEM, and (f),(g) HR TEM micrographs of the undeformed pillar (annealed at 500 °C for about 3 h). Diffraction patterns acquired from the large pillar area in (b) and the upper part of the pillar in (d) do not show an icosahedral structure. The fast Fourier transform (FFT) patterns (Supplemental Material Fig. S1) acquired from the HR TEM regions in (f) and (g) confirm the existence of the Al_3Pd_2 (hP5) phase.

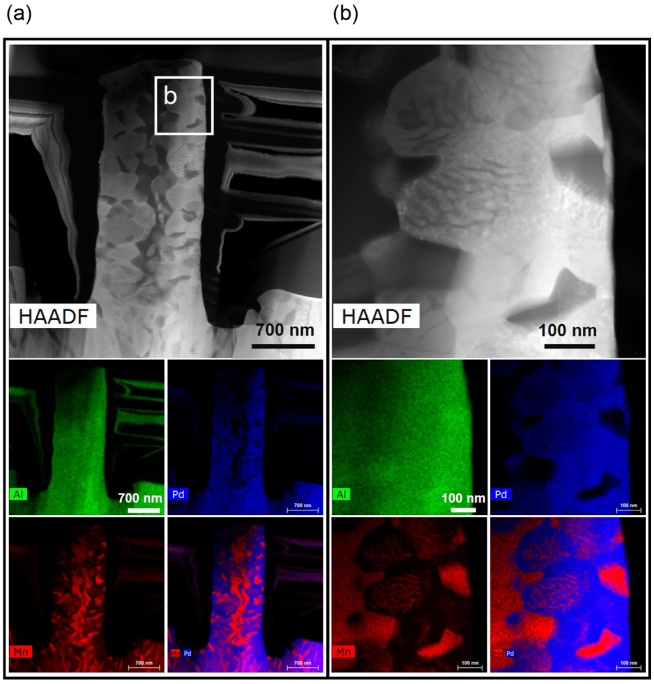

FIG. 6. HAADF STEM micrographs of (a) the whole undeformed pillar annealed at 500 °C and (b) a higher magnification region [square region in Fig. 6(a)], with the corresponding EDS maps showing elemental content distribution.

Compositional analysis of the undeformed pillar annealed at 500 °C was performed using HAADF STEM in combination with EDS spectrum imaging. Figure 6 presents the elemental distribution maps and evidences a nonuniform distribution of Pd and Mn in the pillar. The Al signal shows much fewer modulations through the whole pillar. As shown in Fig. 6(b), Mn-containing regions are also observed within Pd-rich grains, suggesting that phase separation is not complete. The Cliff-Lorimer evaluation algorithm was used to estimate the composition of the Pd-rich and Mn-rich grains. The composition of Mn-rich grains (dark contrast) in Fig. 6(b) is 58 at. % Al, 35 at. % Mn, and 7 at. % Pd; the Pd-rich grains are composed of 53 at. % Al, 45 at. % Pd, and 2 at. % Mn. According to the binary phase diagrams of Al-Pd and Al-Mn alloys, these compositions correlate to Al_8Mn_5 (hR52) in the Mn-rich areas; whereas, in the Pd-rich areas, both AlPd (hR26) and Al_3Pd_2 (hP5) phases are possible. These potential phases correspond well to the diffraction patterns and FFT pattern analyses (Supplemental Material Figs. S1–S3), confirming the thermally induced phase separation process and the existence of multiple binary Al-Pd and Al-Mn phases.

3. Micropillars deformed at 500 °C

Figure 7 presents the TEM micrographs of the pillar deformed at 500 °C, revealing a segregated microstructure similar to that observed in the undeformed pillar in Fig. 5.

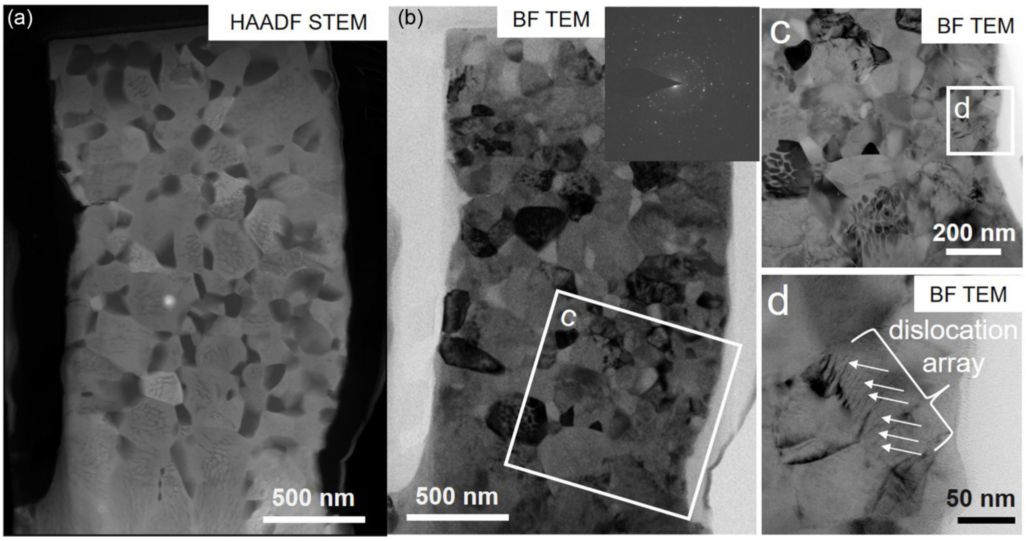

FIG. 7. (a) HAADF STEM, (b) BF TEM with SAED, and (c),(d) enlarged BF TEM views of a pillar compressed at 500 °C, showing the phase separation and grain refinement; (d) dislocations array contrast.

Compared with the undeformed sample, the deformed pillar shows a finer grain size with an average value of $d_{\mathrm{Avg}} = 150\,\mathrm{nm}$, shown in the HAADF STEM [Fig. 7(a)] and BF TEM images [Figs. 7(b)–7(d)]. Again, similar to the undeformed material, the pattern analysis confirms the presence of the icosahedral phase (Supplemental Material Fig. S5). However, due to the limited amount of reflections, the SEAD pattern could match with either i-Al-Mn or i-Al-Pd-Mn systems. Figure S6 shows the measurement of the grain size in deformed/undeformed pillars, indicating grain refinement after compression. The location of segregated grains shows correspondence to the protruding features in SEM images [Fig. 2(f)]. Compared with the undeformed pillar showing a wrinklelike surface [Fig. 3(c)] and large grains (Fig. 5), the deformed pillar might experience a different phase transformation process with a preferred symmetry change under compression [63]. A very thin (~2 nm) oxide layer is observed at the pillar surface (Fig. S7), which might result from the oxidation of aluminum during the sample transfer between characterization steps. Such a thin layer of oxide is not believed to affect the deformation significantly.

The EDS maps (Fig. 8) confirm similar, but more refined, segregation of Mn and Pd in the deformed pillar compared to the undeformed one. In contrast to the undeformed pillar (Fig. 6), Mn clusters in the compressed pillar are distributed more uniformly, forming a large number of fine Mn-rich grains, suggesting that phase separation is more complete. In the higher magnification images [Fig. 8(b)], we observe that fine Mn-rich cluster structures also exist within Pd-rich grains, comparable to those observed in the undeformed pillar. Despite the fine Mn-rich structures observed in the Pd-rich grains, the majority of Mn appears to separate from Pd-rich grains and accumulate at the grain boundary junctions of Pd-rich grains to form pure Al-Mn phases (containing no Pd). This feature indicates that the onset of phase separation may arise from the precipitation of the Mn atoms from the original icosahedral phase, forming binary Al-Mn phases. Moreover, assuming the pattern in Supplemental Material Fig. S5 belongs to i-Al-Mn systems such as $Al_{78}Mn_{22}$ or $Al_{80}Mn_{20}$, the composition of the Mn-rich phase in the compressed pillar suggests that a small concentration of Mn remains within the Pd-rich grains in the form of the icosahedral structure. Hence, the diffusion of Mn may be an important factor in the deformation of i-Al-Pd-Mn at 500 °C.

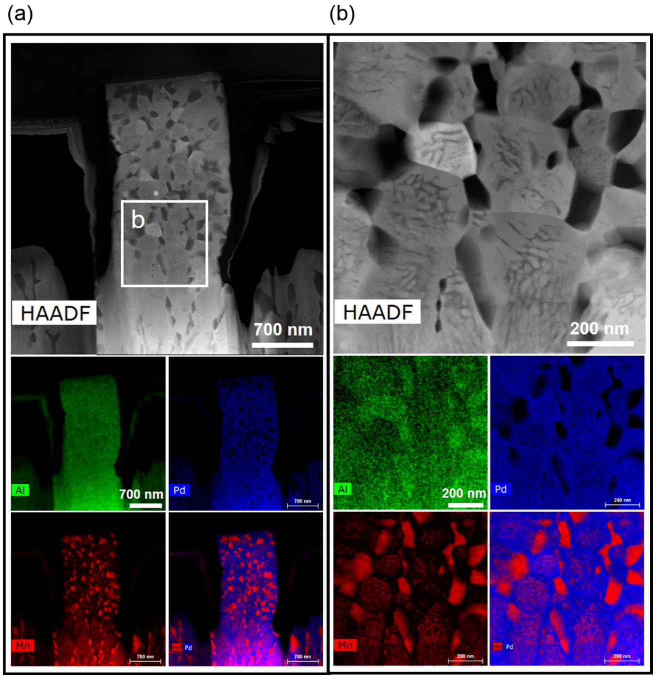

FIG. 8. HAADF STEM micrographs of (a) the deformed pillar annealed at 500 °C and (b) a higher magnification region [the square region in Fig. 8(a)] with the corresponding EDS color maps showing compositional distribution.

TABLE I. Parameters (A, B, and C) in Eq. (2) [66] and calculated saturated vapor pressures (p^o) of Al, Mn, and Pd with corresponding volume change rates ($\dot{n}_{\text{Max}}$) at 500 °C.

Element	A	B	C	p^o (Pa)	$\dot{n}_{\text{Max}}$ (μm^3/h)
Al	9.459	−17342	−0.7927	5.50×10^{-11}	2.03×10^{-5}
Mn	12.805	−15097	−1.7896	1.29×10^{-7}	2.47×10^{-2}
Pd	9.502	−19813	−0.9258	1.59×10^{-14}	2.62×10^{-9}

IV. ANALYSIS AND DISCUSSION

A. Pillar size reduction: Evaporation vs diffusion

As shown in Fig. 3, the pillar size clearly decreased after the 300 and 500 °C annealing stages. Although the densification of the solid due to structural changes, such as phase separation, may lead to the pillar volume reduction, the degree of density disparity is estimated to cause a volume change of less than 1% (calculated from the density of Al_8Mn_5, Al_3Pd_2, AlPd, and i-Al-Pd-Mn [64]), which is much less than the measured volume changes. Thus, crystal structural changes should not be the main reason for the volume changes, and this shrinkage phenomenon could be associated with two probable mechanisms: evaporation and diffusion.

Surface evaporation of Mn in Al-Mn-Pd has been observed in bulk samples, which is reported to produce an enrichment in Pd in the uppermost surface layer [65]. The vapor pressure of Mn is much higher than Al and Pd [66], as shown in Table I, implying Mn evaporates (sublimates) faster than Al and Pd at high temperatures and low pressure (SEM chamber, $\sim 10^{-6}$ Pa). The corresponding evaporation rate of each element can be calculated using the Hertz-Knudsen equation [67,68]:

$$\dot{n}_{\text{Max}} = \frac{p^0}{\sqrt{2\pi MRT}} \quad \text{kmol m}^{-2}\,\text{s}^{-1}, \tag{1}$$

where p^0 is the saturated vapor pressure, M is the molecular weight, R is the universal gas constant, and T is the absolute temperature (in K) at an evaporating surface. The vapor pressure for metallic materials at various temperatures can be calculated as [66]

$$\log_{10} p(\text{atm}) = A + BT^{-1} + C \log_{10} T, \tag{2}$$

where A, B, and C are constants. Table I shows that the evaporation rate of Mn is three orders and seven orders of magnitude higher than that of Al and Pd, respectively, which could lead to the depletion of the Mn from the outer layer of the pillar. However, based on the calculations from Eq. (1), the evaporation rate is not sufficient to cause the observed decrease in size: it would take ~20 h at 500 °C to achieve the measured volume change ($\sim 0.42\,\mu\text{m}^3$) by evaporation alone, whereas the total experiment time at 500 °C during testing was about 2–3 h. It is noted that while intermediate annealing stages at lower temperatures may have contributed to the volume change, the rate of evaporation is much less significant at a lower temperature. Even though the effects of evaporation at different temperatures are accumulated throughout all annealing stages, it is still lower than the observed volume reduction, suggesting the evaporation may not be the primary mechanism. Hence, the secondary mechanism of diffusion is proposed here. The volume diffusivities (i.e., diffusion coefficients) for Pd [69] and Mn [70] in i-Al-Pd-Mn are given below:

$$D_{\text{Pd}} = 1.2 \times 10^{-2} \exp^{\left(-\frac{2.32\,\text{eV}}{kT}\right)}\ \text{m}^2\,\text{s}^{-1}, \tag{3}$$

$$D_{\text{Mn}} = 3.4 \times 10^{-4} \exp^{\left(-\frac{1.88\,\text{eV}}{kT}\right)}\ \text{m}^2\,\text{s}^{-1}. \tag{4}$$

However, to our knowledge, the diffusivity of Al in i-Al-Pd-Mn has not yet been determined in this temperature regime. In a report of self-diffusion of Al in i-Al-Pd-Mn at low temperatures, Dolinšek *et al.* [71] implied that the activation energy (Q) of Al is close to 1.3 eV. To give the best estimation, we use this activation energy value here. Since there are several equations for Al diffusivity [72,73], the one with activation energy close to 1.3 eV is used [74]:

$$D_{\text{Al}} = 0.1 \times 10^{-4} \exp^{\left(-\frac{1.26\,eV}{kT}\right)}\ \text{m}^2\,\text{s}^{-1}. \tag{5}$$

The corresponding diffusivities at 500 °C are calculated from Eqs. (3)–(5) and listed in Table II. However, since the micropillars have a high surface-to-volume ratio, surface diffusion (which has lower activation energy [75]) must also be taken into account. For Mn and Pd, the corresponding activation energies for surface diffusion have been determined to be 0.2 and 0.64 eV, respectively [76]. However, for Al, it varies from 0.054 to 0.69 eV [77], depending on the crystal plane. Here, we use the average of all reported surface diffusivities, as listed in Table II. To calculate the volume change by diffusion, diffusive flux J_i arising from a chemical potential difference can be expressed as [78]

$$J_i = -\frac{Dc_i}{RT}\frac{\partial \mu_i}{\partial x}, \tag{6}$$

where c_i is the concentration (mol/m^3) and $\frac{\partial \mu_i}{\partial x}$ is the gradient of chemical potential (J/mol m). The as-milled pillars have high surface-to-volume ratios and therefore higher surface energy than the substrate, inducing a chemical potential difference. Based on the surface energy of i-Al-Pd-Mn ($28\,\text{mJ/m}^2$ [79,80]), the corresponding rates of volume change caused by the surface diffusion of each element are calculated and listed in Table I. Mn shows the highest surface diffusivity among the three elements, and it is estimated to require about 6 h at 500 °C to achieve the observed volume change solely by the effect of Mn diffusion. It should be noted that this micropillar shrinkage phenomenon has not been reported in pure Al pillars or other Al-based metallic systems that do not contain Mn [50,81]. This is because the difference in activation energies for volume and surface diffusion in Al is relatively small, and thus preferential diffusion of Al along the surface does not noticeably occur.

Combining the effects of evaporation and diffusion, the total volume change rate at 500 °C ($\sim 0.1\,\mu\text{m}^3$/h) corresponds to an annealing time of ~4 h for the measured shrinkage. Since all the pillars experienced the heating processes at elevated temperatures, i.e., 100–500 °C, the volume changes at the previous annealing steps should be taken into account in addition to the effects of evaporation and diffusion at the testing temperature. These combined effects were calculated and are listed in Supplemental Material Table SI [60] and shown graphically in Fig. 9, in which we assume a 2.5-h

TABLE II. Volume and surface diffusion energies and coefficients (diffusivities) of Al, Mn, and Pd and the corresponding volume change rates at 500 °C.

Element	Volume activation energy (eV)	Volume diffusivity (m^2/s)	Surface activation energy (eV)	Surface diffusivity (m^2/s)	Volume change rate ($\mu m^3/h$)
Al	1.26 [74]	6.12×10^{-14} [74]	0.054–0.69 [77]	4.72×10^{-8} [77]	1.82×10^{-3}
Mn	1.88 [70]	1.89×10^{-16} [70]	0.2 [76]	1.69×10^{-5} [76]	6.85×10^{-2}
Pd	2.32 [69]	9.04×10^{-18} [69]	0.64 [76]	8.08×10^{-7} [76]	7.85×10^{-3}

holding time at each temperature. In Fig. 9(a), faster shrinkage occurs at higher temperatures, in which the total rates are calculated as $(2.94, 10.7, 25.1, 47.0, 103) \times 10^{-3}\ \mu m^3/h$ for 100, 200, 300, 400, and 500 °C, respectively; the effect of diffusion is more significant than that of evaporation in all the temperature regimes, especially for the diffusion of Mn along the pillar surface, in which the contribution of Mn diffusion (in the orange solid line) is above 90% of the total diffusion volume change rate (in red dashed line). For example, the rate of volume change due to the Mn diffusion is ~9 and ~38 times faster than those caused by Pd and Al at 500 °C, respectively. Figure 9(b) shows the cumulative volume change at each temperature: the effect of evaporation (in the blue meshed histogram) is apparent only at 500 °C, because the rate of evaporation is negligible below this temperature [in blue dashed line in Fig. 9(a)], corresponding to 13.0% of total volume change; the influence of prior annealing (in the grey meshed histogram, an iteration of the cumulative values at lower temperatures), which is attributed mainly to diffusion, becomes significant at higher temperatures, accounting for 21.6%, 35.2%, 45.1%, and 45.5% of total shrinkage at 200, 300, 400, and 500 °C, respectively. There is good agreement between the calculated volume changes (~0.10 μm^3 at 300 °C and ~0.47 μm^3 at 500 °C) and the measured values (0.14 μm^3 at 300 °C and 0.42 μm^3 at 500 °C).

B. Phase separation and grain refinement: Coupling of temperature and stress

According to the trends in the reported phase diagrams [52], the i-Al-Pd-Mn phase may become increasingly unstable with decreasing temperature. A polycrystalline structure has been observed in bulk i-Al-Pd-Mn compressed at 480 °C [56]. At relatively low temperatures (such as 25 °C), the phase separation might occur too slowly due to the low reaction kinetics, while higher temperatures (such as above 300 °C) may allow the sample to overcome the kinetic limitation, resulting in the phase separation being thermodynamically favorable. The onset of phase transformation above 300 °C was observed in previous studies reported in the literature [61,82]. However, the process may not have been completed due to our short testing time. The incomplete phase transformation is also evidenced by the XRD pattern (Supplemental Material Fig. S8) and SEM characterization (Supplemental Material Fig. S9) of the annealed sample at 300 °C for 2 h. In Fig. S8, the main peaks still represent the icosahedral phases; the existence of AlPd (hR26) indicates that the onset of the phase transformation process in the quasicrystal occurs at 300 °C. The existence of Pd-rich grains also demonstrates the occurrence of incomplete phase transformation after annealing at 300 °C for 2 h (Fig. S9). Whereas when the QC sample was annealed in the elevated temperature regime above 300 and up to 500 °C, the formation of AlPd (hR26), Al_3Pd_2 (hP5), and Al_8Mn_5 (hR52) was observed along with the remaining icosahedral QC phase (Figs. 5 and 6, and Figs. S1–S4 of the Supplemental Material).

The statistical analysis of the grain size distribution in undeformed and compressed pillars in Fig. 10 reveals that d_{Avg} in the compressed pillar (145 ± 75 nm) is smaller than that in the undeformed one (240 ± 83 nm). Such grain refinement can be explained by dynamic recrystallization: when the pillar is compressed, defects (primarily dislocations) are introduced,

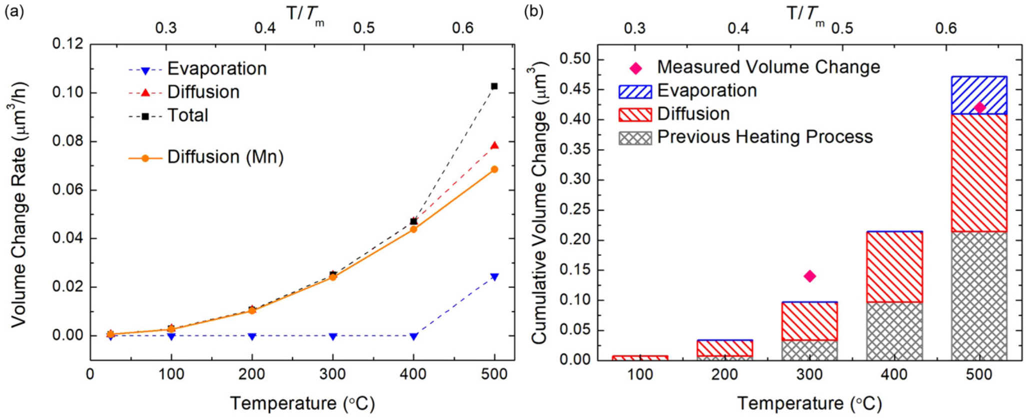

FIG. 9. (a) The calculated volume change rates attributed to the evaporation and surface diffusion of all three elements at different temperatures. (b) The cumulative volume change with the corresponding effects of evaporation and diffusion for 2.5 h testing at each temperature from 100 to 500 °C, composing the volume change due to evaporation, diffusion, and the value of the volume changes in the previous annealing steps. The experimental results for the pillar volume change at 300 and 500 °C are also shown.

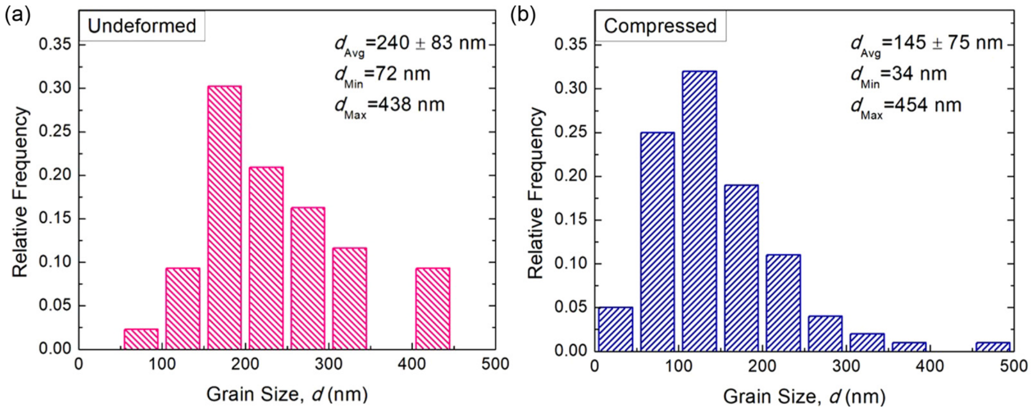

FIG. 10. The grain size distribution of (a) undeformed (annealed) and (b) compressed i-Al-Pd-Mn pillars at 500 °C. The average grain sizes are 240 ± 83 nm and 145 ± 75 nm for undeformed and compressed pillars, respectively.

which can rearrange to form cells, subgrain boundaries, and grain boundaries [83], and can be accompanied by subgrain or nanograin rotation [84]. Such a mechanism can be accelerated at higher temperatures by diffusion-enhanced dislocation motion [85]. Hence, the combination of mechanical and thermal energies at 500 °C would facilitate the formation of refined grains, likely producing the features protruding from the pillar surface, as shown in Fig. 2(f), with similar size to the grain size (∼150 nm).

As compression can induce defects that rearrange into grain boundaries, the grain size can be reduced under compression [86–88]. Generally, the diffusivity through grain boundaries and/or dislocations is much higher than that through the bulk due to the lower activation energies required [75,89]. Via spinodal decomposition, Mn, with its higher volume diffusivity than Pd, will segregate first, diffusing through low-energy pathways and accumulating to form small grains [90,91]. As such, most of the Mn-rich grains at the interfaces of Pd-rich grains exhibit a more uniform distribution in the compressed pillar than the annealed one, as shown in Fig. 8. However, Mn entrapped within the Pd-rich grains has a much lower diffusivity than along interfaces, resulting in the precipitation of fine Mn-rich clusters within Pd-rich grains. Therefore, the deformation of the micropillar deformed at 500 °C enhances both the grain refinement and phase separation, while some quasicrystalline phases still remain after compression (Figs. 7, 8, and S5).

C. Deformation mechanisms of the QC micropillars at 25–500 °C

The stress-strain curves of the i-Al-Pd-Mn pillars compressed at 25 °C [Fig. 2(g)] show almost no plasticity, and the sample morphology [Fig. 2(a)] confirms the brittle fracture behavior. The pillars compressed at higher temperatures exhibit obvious plastic flows with serration behavior, especially below 300 °C [Fig. 11(a)]. Within the temperature in the range 100–300 °C, the flow stress remains roughly constant, but the dynamic flow behavior varies as temperature increases. Above 300 °C, a clear reduction in flow stress is observed. To examine the underlying mechanisms of the serration behavior, we performed a statistical analysis on the force drops of the

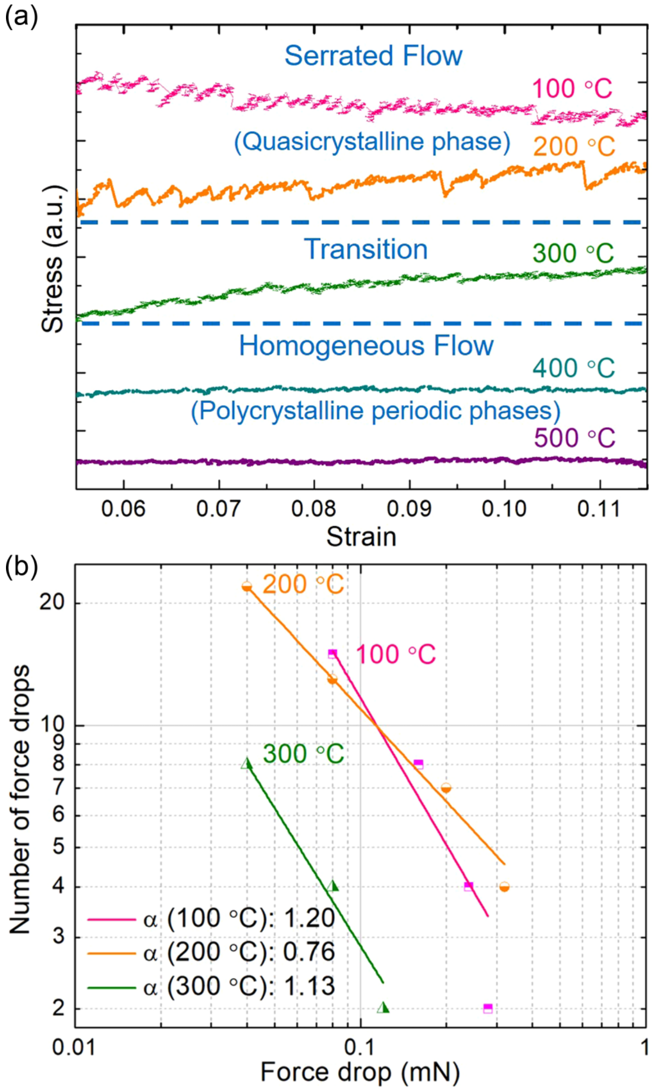

FIG. 11. Statistical analysis of the serration behavior during micropillar compression: (a) illustration of the effect of temperature on the flow behavior. The segments of the stress-strain curves are extracted from Fig. 2. (b) The serration frequency distribution is plotted on logarithmic scales; α refers to the scaling exponent in Eq. (8).

serrations during compression, following a similar procedure to what has been performed on d-Al-Ni-Co [50]. In displacement control, force drops occur when a deformation event relieves strain and elastically unloads the sample [92]. Under a fixed strain rate, the stress drop $\Delta\sigma$ or force drop ΔF is proportional to the velocity of the dislocations, v_{dis}:

$$\Delta F \propto v_{\text{dis}}. \tag{7}$$

Annealing of the bulk sample to 810 °C for 150 h during sample preparation would have yielded a very low initial dislocation density. The serrated plastic flow observed during compression must, therefore, consist of dislocation nucleation, propagation, and annihilation processes.

The number of force drops $n(\Delta F)$ vs the force drop magnitude $|\Delta F|$ from 100 to 300 °C is plotted in Fig. 11(b). These data follow a power-law scaling relationship with a scaling exponent α and a constant C:

$$n(\Delta F) = C|\Delta F|^{-\alpha}, \tag{8}$$

where α is related to the probability of a force drop at a certain magnitude: lower α indicates a higher chance of occurrence of large force drops. Based on Eq. (7), the scaling exponent is thus linked to v_{dis}. Generally, v_{dis} increases as the temperature increases, and therefore α decreases.

From Fig. 11(a), the frequency of the flow serration decreases from 100 to 200 °C and increases from 200 to 300 °C. Additionally, the amplitude of the force drops at 300 °C is much lower than at 200 °C as the serration behavior begins to smooth out, closely resembling the 400 and 500 °C curves. This pattern contradicts most observations in which the force drops increase as temperature increases due to higher v_{dis}. The α values were measured from Fig. 11(b) to be 1.20, 0.76, and 1.13, at 100, 200, and 300 °C, respectively. These results are comparable to previous observations in metal pillars [93], indicating that plastic flow in this temperature range is controlled by dislocation nucleation and propagation. However, the fact that α at 300 °C is much larger than at 200 °C also goes against the trend of decreasing α with increasing temperature as previously reported [50]. These results suggest that multiple deformation mechanisms, in addition to dislocation motion, are at play at 300 °C. The stress-strain curves and deformation morphology at 300 °C [Figs. 2(d) and 2(j)] are thus representative of a transition from serrated flow at relatively low temperatures (100–200 °C) to homogeneous flow at higher temperatures (400–500 °C), which matches well with the occurrence of phase transformation.

To elucidate the dominant deformation mechanisms at each testing temperature, strain-rate jump tests were employed to measure the strain rate sensitivity (SRS), m, represented by [94]

$$m = \frac{\partial \ln \sigma}{\partial \ln \dot{\varepsilon}}, \tag{9}$$

where σ is the flow stress and $\dot{\varepsilon}$ the strain rate. The relation between m and the apparent activation volume V_{a} is shown as [94]

$$V_{\text{a}} = \sqrt{3}\frac{K_B T}{m\sigma}, \tag{10}$$

TABLE III. Calculated strain rate sensitivities (m) with corresponding activation volumes (V_{a}) at various temperatures ($b = 0.183$ nm [44]).

Temperature (°C)	Strain rate sensitivity (m)	Activation volume (V_{a})	
200	0.019 ± 0.015	$0.143 \pm 0.065\ \text{nm}^3$	$24 \pm 11\,b^3$
300	0.036 ± 0.011	$0.096 \pm 0.017\ \text{nm}^3$	$16 \pm 3\,b^3$
400	0.137 ± 0.035	$0.056 \pm 0.009\ \text{nm}^3$	$9 \pm 2\,b^3$
500	0.365 ± 0.036	$0.084 \pm 0.008\ \text{nm}^3$	$14 \pm 2\,b^3$

The activation volume can then be correlated to specific deformation mechanisms generally subdivided into various regimes: diffusion-controlled deformation within the range ~0.1 to 1 b^3; Peierls mechanism from ~10 to 100 b^3; dislocation-solute interactions from 100 to 1000 b^3; and a forest mechanism beyond ~1000 b^3 [85,94]. b is the Burgers vector. Diffusion-based jog dragging, however, can exist over a wide and overlapping range of V_{a} (10 to 1000b^3) [85].

The average values of m were determined from Fig. 12(a) and are presented in Fig. 12(b) and Table III, along with their associated activation volumes. The activation volume at 200 °C has a relatively large range due to its low m value and relatively large error. Nevertheless, the activation volume at 200 °C is close to the bulk value, which ranges from 40 to 245b^3 (640–830 °C, $b = 0.183$ nm) [44], suggesting that dislocation activity is the dominant deformation mechanism. The activation volumes at higher temperatures (300–500 °C) share similar values, indicating that they have similar deformation mechanisms. Obviously, the change of the serrated flow and activation volume at 300 °C suggests that the icosahedral quasicrystal structure is no longer stable and transitions into a regime with new deformation mechanisms. However, as mentioned above, several different mechanisms can exist in a given range V_{a}, and as such, activation volumes are nonspecific indicators and are not sufficient to pin down deformation mechanisms in complex situations [85]. For the single dislocation glide mechanism, V_{a} increases with increasing temperature due to larger dislocation arms/loops; for the transition from dislocation glide to diffusion-based mechanisms, V_{a} may decrease or even remain constant, but that corresponds to a giant increase in activation energy [95]. The activation volume for dislocation glide can also decrease in small-scale specimens due to dislocation arm truncation by the size effect [96]. Thus, the apparent activation energy Q should also be considered to evaluate the corresponding deformation mechanisms at different temperatures.

Q is a parameter devoid of any stress dependence [97], often found in the Arrhenius formulation:

$$\dot{\varepsilon} = A\sigma^n \exp^{(-Q/RT)}, \tag{11}$$

where A is a pre-exponential constant and n is the creep stress exponent. For multiple deformation mechanisms, the one with the lowest Q will control deformation [98]. Based on the studies of Sherby and Armstrong [99], the following equation can be derived from Eq. (11):

$$\sigma = (A^{-1}\dot{\varepsilon})^{1/n} \exp^{(Q/nRT)}. \tag{12}$$

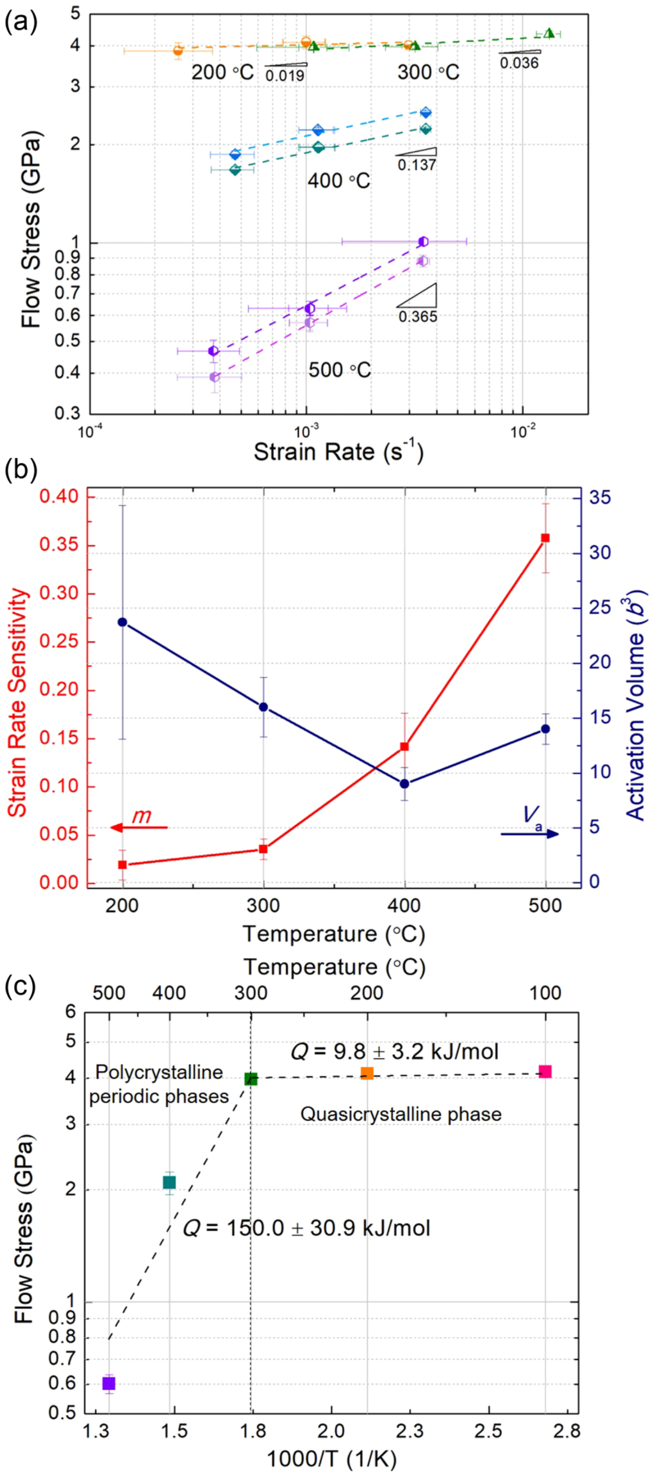

FIG. 12. (a) The flow stress at 5% strain as a function of strain rate, (b) corresponding strain rate sensitivity (m) and activation volume (V_a) for the pillars deformed at 200, 300, 400, and 500 °C, and (c) apparent activation energy (Q) calculated from (flow stress) vs (1000/T) plots. The stress exponent n equals 22 and 4.8 for the deformation temperature below and above 300 °C, respectively.

Therefore, the apparent activation energy for deformation can be calculated from the slope of an $\ln(\sigma)$ vs $(1/T)$ plot, expressed as

$$\ln(\sigma) = B + \frac{Q}{nRT}, \tag{13}$$

where $B = \frac{1}{n}\ln(A^{-1}\dot{\varepsilon})$. Unfortunately, the n value in i-Al-Pd-Mn varies greatly across the literature (from 1 to 6) [43,100–102]. The stress exponent n increases with decreasing deformation temperature [43,102], because the n values are calculated using the following equation: $n = \frac{\partial \ln \dot{\varepsilon}}{\partial \ln \sigma}$ [43]. Here, we obtain the average n values of 22.0 and 4.8 for the deformation temperature below and above 300 °C, respectively, indicating totally different mechanisms in the quasicrystalline and the transformed materials.

Figure 12(c) presents the calculated activation energies, showing two distinct temperature regions. Between 100 and 300 °C, the i-Al-Pd-Mn pillar shows activation energy of ~9.8 kJ/mol, which dramatically increases to ~150 kJ/mol between 300 and 500 °C. These two regions clearly demonstrate two deformation mechanisms, in contrast to what was predicted from the activation volume alone. However, to our knowledge, the activation energies associated with different deformation mechanisms in i-Al-Pd-Mn have not been fully reported.

To categorize the mechanisms, we compare the calculated data with the known activation energies of Al, as Al is homogeneously distributed throughout the pillars and is the element experiencing the highest homologous at temperatures. The low-temperature value of 9.8 kJ/mol correlates to the range for Peierls' stress-dependent or lattice-controlled dislocation glide (7 kJ/mol), which is consistent with the slip offsets observed in Fig. 2 and the measured activation volume. In the high-temperature range, the Q value of 150 kJ/mol aligns with lattice diffusion in Al (142 kJ/mol), corresponding to the Nabarro-Herring creep mechanism [95]. However, we cannot ignore that the presence of Mn and Pd certainly influences the dominant mechanism, even if no activation energy data exist in the literature. Our TEM observations of the pillar compressed at 500 °C (Figs. 7 and 8), show that both dislocation motion and Mn interface diffusion affect deformation, evidenced by the presence of dislocation arrays and grain boundary segregation of Mn, respectively. It should be noted that the grain-boundary segregation and phase separation at higher temperatures (>300 °C) result in complicated co-deformation mechanisms, including dislocation activities of different intermetallic phases, grain-boundary sliding, and diffusion-enhanced plasticity. It is difficult to speculate about the contribution of each possible activity to plasticity. Hence, it is reasonable to believe that dislocation glide is the dominant deformation mechanism at lower temperatures (100–300 °C), while diffusion-enhanced plasticity is the dominant mechanism at higher temperatures (300–500 °C), in which grain boundary rotation/sliding and dislocation motion are also involved. Further, the deformation behavior at 300 °C suggests that both lower and higher temperature mechanisms coexist through this transitional temperature regime.

Figure 13 summarizes the yield stress as a function of temperature for i-Al-Pd-Mn, filling the former gap in data between 25 and 500 °C and demonstrating the deformation mechanisms at elevated temperatures. From RT to 300 °C, the micropillars were still in the QC phase; the deformation of pillars presented a transition from brittle fracture to

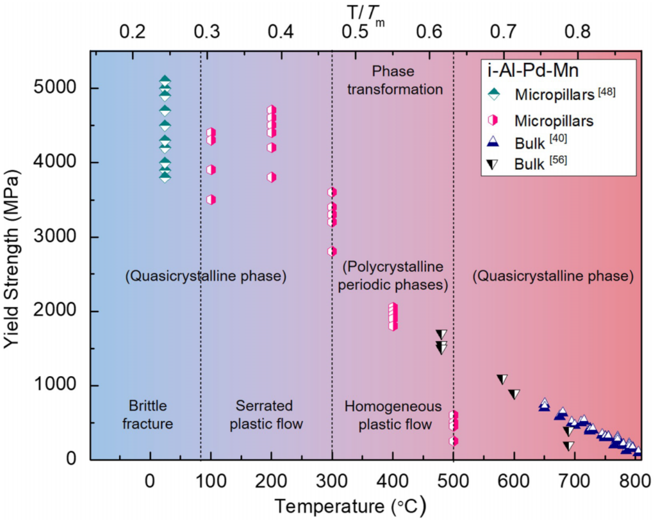

FIG. 13. Yield strength as a function of temperature for the micropillars analyzed in this study (pillar diameter ∼1 μm), previous studies (pillar diameter ∼500 nm at RT) [48], and the bulk materials reported in the literature [40,56]. Three temperature regimes are identified: (i) brittle fracture, (ii) serrated plastic flow, and (iii) homogeneous plastic flow. Phase transformations occur in small-scale samples in the temperature range of approximately 300–500 °C, in which the sample is no longer fully quasicrystalline.

serrated plastic flow. From 300 to 500 °C, the micropillars experienced phase transformation into polycrystalline periodic phases [AlPd (hR26), Al_3Pd_2 (hP5), and Al_8Mn_5 (hR52)]; the homogeneous plastic deformation results from a combination of dislocation, diffusion, and grain boundary rotation/sliding.

Thus, three temperature regimes are identified: (i) brittle fracture, (ii) serrated plastic flow, and (iii) diffusion-enhanced homogeneous flow:

(i) 25 °C (*brittle fracture*): QC micropillars exhibited primarily brittle fracture, with only minimal, localized plasticity.

(ii) 100–300 °C (*serrated plastic flow*): Plastic deformation occurs via dislocation mechanisms during compression with serrated flow characteristics.

(iii) 300–500 °C (*homogeneous plastic flow*): Phase segregation occurs above 300 °C, and the effect of diffusion is significant. The deformation is characterized not only by dislocation activity but also increasingly by diffusion as temperature increases.

V. CONCLUSIONS

In this study, we have explored the deformation behavior of a typically brittle icosahedral quasicrystal, i-Al-Pd-Mn, using elevated temperature microcompression in the previously uninvestigated 25–500 °C temperature range. The main findings are presented as follows:

1. Phase separation and grain refinement are observed in both annealed (undeformed) and compressed micropillars tested above 300 °C. Above 300 °C, the single-quasicrystalline i-Al-Pd-Mn micropillars transformed into polycrystalline structures with multiple, complex phases, including AlPd (hR26), Al_3Pd_2 (hP5), and Al_8Mn_5 (hR52). External stress induced additional defects into the micropillar, resulting in further grain refinement (from ∼250 to ∼150 nm in average grain size) and phase separation through stress-assisted diffusion of Mn along grain/phase boundaries. As such, applications that seek to use i-Al-Pd-Mn for its strength must limit their operating temperatures to below 300 °C.

2. In the temperature range from 25 to 500 °C, clear transitions in deformation behavior were observed. From room temperature to 300 °C, our observed mechanical behavior is based on the quasicrystalline Al-Pd-Mn phase; from 300 to 500 °C, the mechanical behavior is based on the transformed polycrystalline intermetallic phases. (i) At room temperature, the i-Al-Pd-Mn micropillars exhibited brittle fracture with very localized plasticity. (ii) From 100 to 300 °C, the micropillars exhibited serrated plastic flows, suggesting their plastic deformation is dominated by dislocation motion. (iii) From 300 to 500 °C, the single-quasicrystalline phase transformed into ultrafine grains with complex intermetallic phases; their homogeneous plastic deformation occurred by a combination of mechanisms including diffusion, dislocation activity, and grain boundary rotation/sliding.

ACKNOWLEDGMENTS

The authors thank Dr. A. S. Sologubenko (The Scientific Center for Optical and Electron Microscopy, ETH Zurich), Prof. R. Spolenak, and Prof. W. Steurer (ETH Zurich) for their support and helpful discussion. Y.Z. acknowledges the financial support from the Discovery Grants Program (Grant No. RGPIN-2018-05731) of the Natural Sciences and Engineering Research Council of Canada (NSERC) and Dean's Spark Assistant Professorship in the Faculty of Applied Science & Engineering at the University of Toronto.

---

[1] D. Shechtman, I. Blech, D. Gratias, and J. W. Cahn, Phys. Rev. Lett. **53**, 1951 (1984).

[2] T. Janssen, *International Tables for Crystallography*, 2nd ed., Volume D: Physical properties of crystals, Part 1. Tensorial aspects of physical properties (John Wiley & Sons, Inc., 2013), Chap. 1.10, pp. 246–270.

[3] V. Elser, Phys. Rev. B **32**, 4892 (1985).

[4] M. Widom, K. J. Strandburg, and R. H. Swendsen, Phys. Rev. Lett. **58**, 706 (1987).

[5] J. E. S. Socolar, Phys. Rev. B **39**, 10519 (1989).

[6] G. Grosso and G. P. Parravicini, in *Solid State Physics*, 2nd ed., edited by G. Grosso and G. P. Parravicini (Academic, Amsterdam, 2014), pp. 67–105.

[7] W. Steurer and T. Haibach, *International Tables for Crystallography*, 2nd ed., Volume B: Reciprocal space, Part 4. Diffuse scattering and related topics (John Wiley & Sons, Inc., 2010), Chap. 4.6, pp. 590–624.

[8] S. Ranganathan, K. Chattopadhyay, A. Singh, and K. F. Kelton, Prog. Mater Sci. **41**, 195 (1997).

[9] A. P. Tsai, Sci. Technol. Adv. Mater. **9**, 013008 (2008).

[10] V. Elser and C. L. Henley, Phys. Rev. Lett. **55**, 2883 (1985).

[11] Christopher, L. Henley, and V. Elser, Philos. Mag. B **53**, L59 (1986).

[12] A.-P. Tsai, A. Inoue, and T. Masumoto, Jpn. J. Appl. Phys. **26**, L1505 (1987).

[13] A. Goldman and M. Widom, Annu. Rev. Phys. Chem. **42**, 685 (1991).

[14] H. Takakura, C. P. Gomez, A. Yamamoto, M. De Boissieu, and A. P. Tsai, Nat. Mater. **6**, 58 (2007).

[15] Y. K. Vekilov and M. A. Chernikov, Phys. Usp. **53**, 537 (2010).

[16] A.-P. Tsai, Acc. Chem. Res. **36**, 31 (2003).

[17] L. Bindi, P. J. Steinhardt, N. Yao, and P. J. Lu, Science **324**, 1306 (2009).

[18] L. Bindi, N. Yao, C. Lin, L. S. Hollister, C. L. Andronicos, V. V. Distler, M. P. Eddy, A. Kostin, V. Kryachko, G. J. MacPherson, W. M. Steinhardt, M. Yudovskaya, and P. J. Steinhardt, Sci. Rep. **5**, 9111 (2015).

[19] K. Urban, M. Feuerbacher, and M. Wollgarten, MRS Bull. **22**, 65 (1997).

[20] K. Urban, M. Wollgarten, and R. Wittmann, Phys. Scr. **1993**, 360 (1993).

[21] J. Dubois, S. Kang, and J. V. Stebut, J. Mater. Sci. Lett. **10**, 537 (1991).

[22] J. M. Dubois, S. S. Kang, and Y. Massiani, J. Non Cryst. Solids **153-154**, 443 (1993).

[23] V. Demange, A. Milandri, M. De Weerd, F. Machizaud, G. Jeandel, and J. Dubois, Phys. Rev. B **65**, 144205 (2002).

[24] R. M. Stroud, A. M. Viano, P. C. Gibbons, K. F. Kelton, and S. T. Misture, Appl. Phys. Lett. **69**, 2998 (1996).

[25] M. Chernikov, A. Bernasconi, C. Beeli, A. Schilling, and H. Ott, Phys. Rev. B **48**, 3058 (1993).

[26] M. Chernikov, A. Bianchi, and H. Ott, Phys. Rev. B **51**, 153 (1995).

[27] F. Hippert, M. Audier, J. Préjean, A. Sulpice, E. Lhotel, V. Simonet, and Y. Calvayrac, Phys. Rev. B **68**, 134402 (2003).

[28] L. Degiorgi, M. Chernikov, C. Beeli, and H. Ott, Solid State Commun. **87**, 721 (1993).

[29] E. Huttunen-Saarivirta, J. Alloys Compd. **363**, 154 (2004).

[30] Z. M. Stadnik, *Physical Properties of Quasicrystals*, Springer Series in Solid-State Sciences, Vol. 126 (Springer, Berlin, Heidelberg, 2012).

[31] M. Feuerbacher and P. Schall, Scr. Mater. **49**, 25 (2003).

[32] K. Edagawa, S. Ohta, S. Takeuchi, E. Kabutoya, J. Guo, and A.-P. Tsai, Mater. Science Eng. A **294**, 748 (2000).

[33] M. Wollgarten, H. Saka, and A. Inoue, Philos. Mag. A **79**, 2195 (1999).

[34] F. Mompiou and D. Caillard, Acta Mater. **52**, 3613 (2004).

[35] J. E. S. Socolar, T. C. Lubensky, and P. J. Steinhardt, Phys. Rev. B **34**, 3345 (1986).

[36] M. Feuerbacher, Chem. Soc. Rev. **41**, 6745 (2012).

[37] K. Edagawa, Mater. Sci. Eng. A **309**, 528 (2001).

[38] M. de Boissieu, Chem. Soc. Rev. **41**, 6778 (2012).

[39] M. Feuerbacher, C. Metzmacher, M. Wollgarten, K. Urban, B. Baufeld, M. Bartsch, and U. Messerschmidt, Mater. Sci. Eng. A **226-228**, 943 (1997).

[40] M. Feuerbacher, C. Metzmacher, M. Wollgarten, K. Urban, B. Baufeld, M. Bartsch, and U. Messerschmidt, Mater. Sci. Eng. A **233**, 103 (1997).

[41] F. Mompiou and D. Caillard, Acta Mater. **56**, 2262 (2008).

[42] F. Mompiou and D. Caillard, C. R. Phys. **15**, 82 (2014).

[43] U. Messerschmidt and M. Bartsch, Scr. Mater. **49**, 33 (2003).

[44] U. Messerschmidt, M. Bartsch, M. Feuerbacher, B. Geyer, and K. Urban, Philos. Mag. A **79**, 2123 (1999).

[45] D. Caillard, F. Mompiou, L. Bresson, and D. Gratias, Scr. Mater. **49**, 11 (2003).

[46] Y. Yokoyama, A. Inoue, and T. Masumoto, Mater. Trans., JIM **34**, 135 (1993).

[47] L. Bresson and D. Gratias, J. Non Cryst. Solids **153**, 468 (1993).

[48] Y. Zou, P. Kuczera, A. Sologubenko, T. Sumigawa, T. Kitamura, W. Steurer, and R. Spolenak, Nat. Commun. **7**, 12261 (2016).

[49] Y. Zou, P. Kuczera, W. Steurer, and R. Spolenak, Extreme Mech. Lett. **8**, 229 (2016).

[50] Y. Zou, J. M. Wheeler, A. S. Sologubenko, J. Michler, W. Steurer, and R. Spolenak, Philos. Mag. **96**, 3356 (2016).

[51] V. Raghavan, J. Phase Equilib. Diffus. **30**, 71 (2009).

[52] S. Balanetskyy, G. Meisterernst, M. Heggen, and M. Feuerbacher, Intermetallics **16**, 71 (2008).

[53] M. Texier, A. Proult, J. Bonneville, J. Rabier, N. Baluc, and P. Cordier, Philos. Mag. Lett. **82**, 659 (2002).

[54] M. Texier, A. Proult, J. Bonneville, J. Rabier, N. Baluc, and P. Cordier, Scr. Mater. **49**, 47 (2003).

[55] M. Texier, A. Proult, J. Bonneville, and J. Rabier, Mater. Sci. Eng. A **387-389**, 1023 (2004).

[56] M. Texier, L. Thilly, J. Bonneville, A. Proult, and J. Rabier, Mater. Sci. Eng. A **400**, 311 (2005).

[57] M. Texier, A. Joulain, J. Bonneville, L. Thilly, and J. Rabier, Philos. Mag. **87**, 1497 (2007).

[58] J. R. Greer, W. C. Oliver, and W. D. Nix, Acta Mater. **53**, 1821 (2005).

[59] Y. Shibutani, T. Tsuru, and A. Koyama, Acta Mater. **55**, 1813 (2007).

[60] See Supplemental Material at http://link.aps.org/supplemental/10.1103/PhysRevMaterials.5.053602 for (Figs. S1–S6) TEM images with SAED and FFT patterns of deformed/undeformed pillars at 500 °C, (Fig. S7) oxygen and carbon distributions, (Fig. S8) XRD, and (Fig. S9) SEM-EDS results of 300 °C-annealed bulk sample, and (Table SI) calculated volume change rates from 100 to 500 °C.

[61] Z. Shen, C. J. Jenks, J. Anderegg, D. Delaney, T. A. Lograsso, P. A. Thiel, and A. Goldman, Phys. Rev. Lett. **78**, 1050 (1997).

[62] A. Tsai, A. Inoues, Y. Yokoyama, and T. Masumoto, Philos. Mag. Lett. **61**, 9 (1990).

[63] G. Mettela, Y. A. Sorb, A. Shukla, C. Bellin, V. Svitlyk, M. Mezouar, C. Narayana, and G. U. Kulkarni, Chem. Mater. **29**, 1485 (2017).

[64] K. Tanaka, Y. Mitara, and M. Koiwa, Philos. Mag. A **73**, 1715 (1996).

[65] P. Ebert, F. Kluge, B. Grushko, and K. Urban, Phys. Rev. B **60**, 874 (1999).

[66] C. Alcock, V. Itkin, and M. Horrigan, Can. Metall. Q. **23**, 309 (1984).

[67] J. Safarian and T. A. Engh, Metall. Mater. Trans. A **44**, 747 (2013).

[68] S. Dushman and J. M. Lafferty, and Research Staff of General Electric Research Laboratory, Am. J. Phys. **30**, 612 (1962).

[69] R. Blüher, P. Scharwaechter, W. Frank, and H. Kronmüller, Phys. Rev. Lett. **80**, 1014 (1998).

[70] W. Sprengel, T. A. Lograsso, and H. Nakajima, Phys. Rev. Lett. **77**, 5233 (1996).

[71] J. Dolinšek, T. Apih, M. Simsič, and J. Dubois, Phys. Rev. Lett. **82**, 572 (1999).

[72] T. Lundy and J. Murdock, J. Appl. Phys. **33**, 1671 (1962).

[73] G. Neumann and C. Tuijn, *Self-Diffusion and Impurity Diffusion in Pure Metals*, Handbook of Experimental Data (Elsevier Science, New York, 2011).

[74] S. Dais, R. Messer, and A. Seeger, *Vacancies and Interstitials in Metals and Alloys*, Materials Science Forum, Vol. 15 (Trans Tech Publications Ltd, 1987), pp. 419–424.

[75] J. C. Fisher, J. Appl. Phys. **22**, 74 (1951).

[76] F. Samavat, M. Gladys, C. Jenks, T. Lograsso, B. King, and D. O'Connor, Surf. Sci. **601**, 5678 (2007).

[77] C. Liu, J. Cohen, J. Adams, and A. Voter, Surf. Sci. **253**, 334 (1991).

[78] A. Paul and S. Divinski, *Diffusion Fundamentals and Techniques*, Handbook of Solid State Diffusion Vol. 1 (Elsevier, Saint Louis, 2017).

[79] C. J. Jenks and P. A. Thiel, MRS Bull. **22**, 55 (1997).

[80] D. J. Sordelet and J. M. Dubois, MRS Bull. **22**, 34 (1997).

[81] T. E. J. Edwards, F. Di Gioacchino, A. J. Goodfellow, G. Mohanty, J. Wehrs, J. Michler, and W. J. Clegg, Acta Mater. **166**, 85 (2019).

[82] R. Lück, T. Gödecke, and C. Beeli, MRS Online Proc. Libr. **643**, 241 (2000).

[83] D. Hull and D. J. Bacon, *Introduction to Dislocations*, 4th ed. (Butterworth-Heinemann, Oxford, 2001).

[84] B. B. Rath, M. Winning, and J. Li, Appl. Phys. Lett. **90**, 161915 (2007).

[85] U. Messerschmidt, *Dislocation Dynamics During Plastic Deformation* (Springer-Verlag, Berlin, Heidelberg, 2010), Vol. 129.

[86] A. Ardell and S. Prikhodko, Acta Mater. **51**, 5013 (2003).

[87] N. Starostina, S. Prikhodko, A. Ardell, and S. Prasad, Mater. Sci. Eng. A **397**, 264 (2005).

[88] X. Tong, Y. Li, Z. Yan, D. Wang, and S. Shi, J. Mater. Res. Technol. **9**, 2063 (2019).

[89] P. Heitjans and J. Kärger, *Diffusion in Condensed Matter: Methods, Materials, Models* (Springer, Berlin, Heidelberg, 2006).

[90] J. Chen, L. Zou, Y. Chen, and Q. Li, Mater. Sci. Technol. **32**, 77 (2016).

[91] L. Zhu, Y. Li, S. Shi, Z. Yan, J. Chen, and S. Maqbool, Nanomaterials **9**, 294 (2019).

[92] M. D. Uchic, P. A. Shade, and D. M. Dimiduk, Annu. Rev. Mater. Res. **39**, 361 (2009).

[93] D. M. Dimiduk, C. Woodward, R. LeSar, and M. D. Uchic, Science **312**, 1188 (2006).

[94] D. Caillard and J.-L. Martin, *Thermally Activated Mechanisms in Crystal Plasticity* (Elsevier Science, New York, 2003).

[95] J. Wheeler, V. Maier, K. Durst, M. Göken, and J. Michler, Mater. Sci. Eng. A **585**, 108 (2013).

[96] Y. Xiao, Y. Zou, A. S. Sologubenko, R. Spolenak, and J. M. Wheeler, Mater. Des. **193**, 108786 (2020).

[97] G. Mohanty, J. M. Wheeler, R. Raghavan, J. Wehrs, M. Hasegawa, S. Mischler, L. Philippe, and J. Michler, Philos. Mag. **95**, 1878 (2015).

[98] F. Garofalo, *Fundamentals of Creep and Creep-rupture in Metals* (Macmillan, New York, 1965).

[99] O. Sherby and P. Armstrong, Metall. Mater. Trans. B **2**, 3479 (1971).

[100] J. Shield, M. Kramer, and R. McCallum, J. Mater. Res. **9**, 343 (1994).

[101] M. Feuerbacher, B. Baufeld, R. Rosefeld, M. Bartsch, G. Hanke, M. Beyss, M. Wollgarten, U. Messerschmidt, and K. Urban, Philos. Mag. Lett. **71**, 91 (1995).

[102] H.-R. Trebin, *Quasicrystals: Structure and Physical Properties* (Wiley-VCH, Weinheim, 2003).